Nanoscale

COMMUNICATION

View Article Online
View Journal | View Issue

Cite this: *Nanoscale*, 2025, **17**, 3053

Received 26th July 2024,
Accepted 27th November 2024

DOI: 10.1039/d4nr03091e

rsc.li/nanoscale

Polarisation-dependent Raman enhancement in hexagonal boron nitride membranes†

Jakub Rogoża, [a] Johannes Binder, *[a] Kirill V. Voronin, [b] Iris Niehues, [c,d] Katarzyna Ludwiczak,[a] Aleksandra K. Dąbrowska,[a] Mateusz Tokarczyk,[a] Rafał Bożek,[a] Alexey Y. Nikitin,[b,e] Rainer Hillenbrand,[c,e] Roman Stępniewski [a] and Andrzej Wysmołek[a]

Raman spectroscopy is a powerful analytical method widely used in many fields of science and applications. However, one of the inherent issues of this method is a low signal-to-noise ratio for ultrathin and two-dimensional (2D) materials. To overcome this problem, techniques like surface-enhanced Raman spectroscopy (SERS) that rely on nanometer scale metallic particles are commonly employed. Here, we demonstrate a different approach that is based on a microcavity structure consisting of a hexagonal boron nitride (h-BN) membrane spanning over an air-filled trench in germanium. In this structure, the h-BN membrane is an integral part of the cavity and, at the same time, shows an about 10-fold, polarisation-dependent h-BN Raman signal enhancement. With h-BN being transparent, flat, and chemically robust, it provides an excellent interface between the cavity and adjacent materials. We show that the Raman enhancement is also present for graphene layers transferred on top of the h-BN membrane, which proves that our approach can be extended to van der Waals heterostructures. The observed polarisation and position-dependent enhancements are in very good agreement with numerical simulations of the electric field intensity of the cavity. These results, together with the presented facile h-BN membrane fabrication process, which does not require any lithographic methods, open up new possibilities for enhancing Raman signals of 2D crystals without the need for metal particles.

Introduction

Raman spectroscopy is a workhorse technique that serves in many aspects of our lives. Despite being used in natural sciences, Raman spectroscopy is also used in medical applications,[1–4] as a tool for tracking illegal substances[5–8] and as a method of quality control in industry.[9–12] One of the drawbacks of Raman spectroscopy is a poor signal to noise ratio for example for ultrathin and 2D materials or delicate matter for which only very low laser excitation powers can be used. In such cases, Raman enhancement techniques like surface-enhanced Raman spectroscopy (SERS)[13–15] or Tip-Enhanced Raman Spectroscopy (TERS)[16–18] can be employed to mitigate these problems. Although these techniques are widely used, they also have disadvantages, like a large roughness of typical substrates used for SERS or the fact that SERS techniques require metallic surfaces. The application of metals can produce additional electrochemical effects and change the properties or even destroy the examined samples.[19] One way to address this issue is to use shell-isolated nanoparticle-enhanced Raman spectroscopy (SHINERS). In this method, the metal nanoparticles are covered with an ultrathin dielectric coating that prevents direct contact with the metal while still allowing for Raman signal enhancement.[20,21] When flat surfaces are required, nanoparticle-based methods are not suitable. In this case, Interference Enhanced Raman Scattering (IERS)[22–25] has been employed, where enhancement is achieved through interference effects on mirror-like substrates coated with a dielectric.

Here, we present an approach that goes further by utilizing a microcavity structure that consists of a hexagonal boron nitride (h-BN) layer suspended over an air-filled trench etched into germanium. With our original fabrication technique, we can create germanium/h-BN membrane microcavities of various shapes directly by laser illumination using a standard Raman spectroscopy system. The simplicity of this technique allows for the fabrication of micrometer sized membranes, without applying lithographic techniques.

In our cavity structure, the h-BN membrane plays a two-fold role. Firstly, it is an integral part of the micro-cavity and therefore essential to achieve enhanced electric fields. We directly

[a]*University of Warsaw, Faculty of Physics, Pasteura 5, 02-093 Warsaw, Poland*
[b]*Donostia International Physics Center (DIPC), Paseo Manuel de Lardizabal, 4, Donostia-San Sebastián 20018, Spain. E-mail: johannes.binder@fuw.edu.pl*
[c]*CIC nanoGUNE BRTA and Department of Electricity and Electronics, UPV/EHU, Tolosa Hiribidea, 76, Donostia-San Sebastián 20018, Spain*
[d]*University of Münster, Institute of Physics, Wilhelm-Klemm-Str. 10, 48149 Münster, Germany*
[e]*IKERBASQUE, Basque Foundation for Science, Bilbao 48009, Spain*
† Electronic supplementary information (ESI) available. See DOI: https://doi.org/10.1039/d4nr03091e

observe this field enhancement as an increase in the Raman signal of the suspended h-BN itself. Secondly, it can be used as a flat, insulating[26–29] platform to increase the Raman signal of other 2D materials that are placed on top of the membrane, as we demonstrate for the case of a h-BN/graphene heterostructure. The choice of h-BN as an interfacing material provides us with the great advantage of using a chemically stable,[30] insulating material that does not interact chemically with an adjacent sample. Moreover, h-BN is transparent in the visible spectral range, allowing us to construct mechanically robust cavity structures based on thicker layers (30 nm in our case). Finally, h-BN is known to be an excellent substrate for other 2D materials[31–33] and hence is the platform of choice for enhancing Raman signals of 2D materials in van der Waals heterostructures.

Experimental details

Hexagonal boron nitride (h-BN) was grown by Metalorganic Vapour-Phase Epitaxy (MOVPE) with an Aixtron CCS 3 × 2-inch reactor. In this work, a continuous layer, with a thickness of about 30 nm, was grown by two stage epitaxy at a temperature of 1300 °C using ammonia and triethylboron (TEB) as precursors and hydrogen as carrier gas.[34] As a substrate 2-inch *c*-plane Al_2O_3 wafers with a 1° off-cut angle were used.[35]

To obtain membranes, we adapt a photocorrosion technique that we initially developed to directly underetch graphene grown on germanium.[36] The process involves a transfer of the h-BN from the sapphire substrate onto a bulk germanium substrate using a wet delamination technique:[37] the sample was carefully immersed in deionized water to initiate the delamination of the h-BN epilayer from the sapphire substrate. As a result, h-BN floats on the water surface and can be transferred onto a germanium substrate that was also immersed in the water bath.

To remove excess water after the transfer, an initial drying step on a hot plate was carried out. The temperature was set to 80 °C to prevent boiling of the water, which could potentially damage the h-BN layer. The sample remained on the hot plate for approximately three hours. Subsequently, the sample was transferred to a vacuum oven for further processing. The vacuum oven was set to 100 °C, and the sample was kept under vacuum conditions for approximately 24 hours. This step ensured that the sample became resistant to further delamination during the etching process.

To prepare micro-membranes, we etch the germanium beneath the h-BN layer. To this end, we make use of a photocorrosion process that leads to an oxidation of the germanium layer upon exposure to water and a focused light source.[36] The oxidized germanium dissolves in water and is removed from the etched area. As a result, we are able to directly write trenches into germanium without affecting the transparent h-BN above. An advantage of this technique is that no lithographic processing or careful alignment of layers is needed, as would be the case with a typical stamp-based transfer onto a predefined substrate. Moreover, our technique yields largely unstrained layers (see ESI†), which is difficult to achieve with other methods.

For exposure, we utilize a Renishaw InVia Raman system equipped with a translational stage offering a spatial resolution of 100 nm. The etching process is performed with a continuous wave laser (532 nm) used for standard Raman spectroscopy with a power of 30 mW. A water dipping objective (NA 0.8) with 40× magnification is used. The objective is directly immersed in the water.

To initiate the etching, the sample is first placed in a dish filled with deionised water. The process begins by exposing a point on the germanium surface that is not covered by h-BN. Subsequently, the spot is incrementally moved by 100 nm, allowing for the etching of a trench in the germanium layer. Once the spot reaches the area where the germanium is covered by the h-BN layer, the h-BN transmits the light, which is crucial for the photocorrosion to take place. It is essential to maintain small and precise steps during the etching process to ensure the continuity of the etched trench. This continuity is crucial for enabling water to reach the currently etched region of the germanium.

Results and discussion

We fabricated h-BN membranes on a Ge substrate in the form of a grid structure with a distance of 10 μm between neighbouring lines. Fig. 1(a) schematically illustrates the etching process. Optical and scanning electron microscope (SEM)

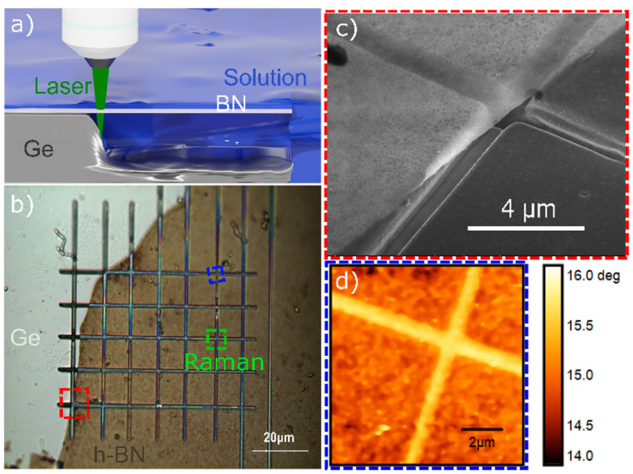

Fig. 1 (a) Three-dimensional illustration of the etching process that leads to a trench in germanium beneath the h-BN layer. (b) Optical phase contrast image of an etched grid structure. The red square marks the region shown in the SEM image in (c). The blue square indicates the region where the AFM image in (d) was measured, and the green area corresponds to the Raman maps shown in Fig. 2(c and d). (c) SEM image that demonstrates the smoothness of the trench etches. (d) AFM phase contrast image, used to extract the dimensions of the trench.

images of the structure are shown in Fig. 1(b) and (c). In Fig. 1(c) one can see that a step of 100 nm yields almost continuous well-defined trenches with sharp edges. Importantly, the h-BN surface is not damaged in any way during the process, consistent with what has been shown for graphene membranes fabricated using the photocorrosion method.[36] Fig. 1(d) shows an atomic force microscope (AFM) phase contrast measurement in noncontact mode on which the etched trenches (bright areas) can be clearly observed. By averaging several sections of the map, the width of the edged trench was estimated to be around 1.3 μm.

To investigate the optical properties of the obtained microcavity structures, Raman mapping was conducted under ambient conditions using the same equipment as used for membrane fabrication with a linearly polarized laser excitation (532 nm). Prior to the measurements the samples were carefully dried to make sure that no further photocorrosion occurs. The incident laser polarization was altered using a half-wave plate. No polarization optics were employed for light detection. The mapping was performed using a 100 nm step size with a microscope objective with a 100× magnification (NA 0.85). The laser power was 30 mW on the sample for measurements of hBN. Fig. 2(a) shows typical spectra taken on suspended h-BN, close to the edge of the membrane (black curve) and on h-BN supported by the germanium substrate (red curve). Both, the second-order Raman signals from germanium[38] (400–600 cm^{-1}) and the E_{2g} peak from h-BN[39] (1367 cm^{-1}) are visible in the spectrum, with a significant enhancement of the h-BN Raman signal close to the edges of the trenches. Both spectra were taken at the locations indicated on the map in Fig. 2(d). Fig. 2(c) and (d) present the maps obtained by fitting a Lorentzian peak function to the Raman h-BN band (maps of Raman shift and FWHM are presented in the ESI†). The mapped areas are indicated by a green dashed square in Fig. 1b.

A luminescence background, which originates from point defects in h-BN,[40] was removed before fitting. This background is related to point defects in the h-BN layer that are introduced during the growth and is not related to the membrane fabrication process. The maps were measured using different linear polarizations of the laser, as marked in Fig. 2(c) and (d). The data indicate that the enhancement of the Raman signal from the hBN membrane is highly dependent on the polarization of the excitation laser. The signal is more intense for a polarisation parallel to the edge of the trench. Fig. 2(b) shows a cross-section of the map from panel (d) (indicated by a black, dashed line). The intensities corresponding to the E_{2g} band of h-BN (black line) and the 2nd order germanium signal (red line) for reference. In can be clearly seen that the Raman signal of h-BN shows two distinct maxima close to the edges of the trench. For these points the signal is enhanced by a factor of ~10. Between the maxima, the signal decreases but is still higher than for the suspended regions next to the trench. Importantly, the second order Raman signal of germanium shows the expected behavior related to the geometrical shape of the etched trench and is not enhanced at any point. The

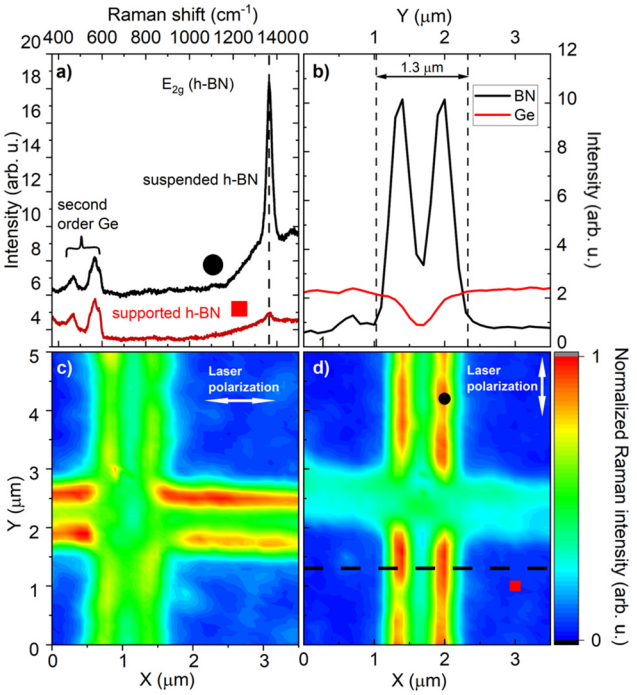

Fig. 2 (a) Typical Raman spectra for two characteristic regions. The black curve represents a spectrum measured close to the edge of the membrane, and the red spectrum a point far from the membrane. Both spectra display a second order signal from germanium and the E_{2g} band from h-BN. (b) Intensity cross-section of the Raman bands from h-BN and germanium. The spatial position of the cross section is indicated by a dashed line in (c). False colour Raman intensity map of the E_{2g} band with a laser polarisation set parallel to the *X* axis. (d) Raman map obtained for the h-BN band, measured with the laser polarisation parallel to the *Y* axis. The red square and black circle indicate the measurement locations for the spectra shown in (a). The maps clearly show that a Raman enhancement occurs when the laser polarisation is parallel to the sidewall of the trench.

black dashed lines in Fig. 2(b) represent the average width of the trench, which was determined from AFM measurements. By comparing the positions of the maxima with the trench one can conclude that the maximum signal from h-BN is detected on the membrane, close to the edge of the trench. However, the actual shape of the maximum is also influenced by the finite size of our laser spot (~500 nm). Fig. 2(c) shows that although the main enhancement is present at the edge oriented parallel to the laser polarization, there is a small enhancement visible also for the perpendicular edge.

To study whether we can extend our fabrication method to van der Waals heterostructures, we first transferred bilayer graphene on top of the h-BN and consecutively fabricate the grid structure from the h-BN/graphene sample shown in Fig. 3(a) using the same photocorrosion etching procedure as described before. The graphene was transferred form large area CVD graphene samples on copper. First the copper was etched in ammonium persulfate and then the graphene was transferred onto the h-BN on germanium by using a PDMS frame.[41,42]

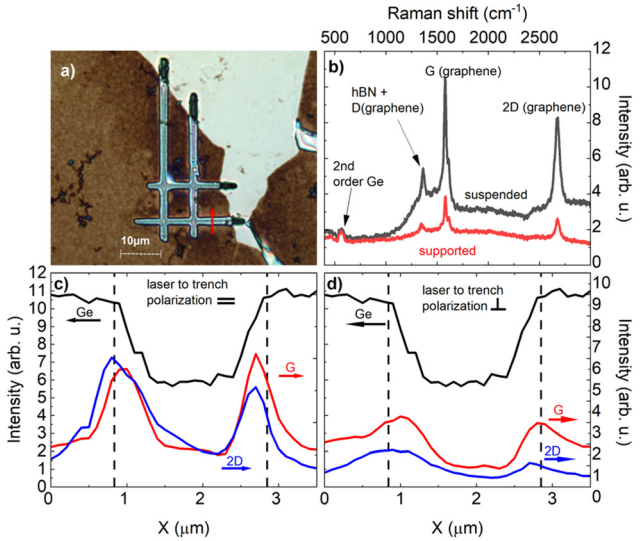

Fig. 3 (a) Phase-contrast optical microscope image of a structure comprising a graphene bilayer on h-BN on a germanium substrate. (b) Raman spectra measured on the membrane edge and on a supported graphene/h-BN region. The Raman lines from graphene (G and 2D), the E_{2g} line from h-BN, and the second order from germanium are marked on the spectra. (c) Raman intensity of the graphene bands (G, 2D) measured across a line indicated by the red arrow in figure (a). The laser was polarised parallel to the trench. (d) Raman intensity cross-section similar to figure (c), with the laser polarisation perpendicular to the trench. Dashed lines indicate the width of the measured membranes. These measurements demonstrate that a Raman enhancement is also present for graphene.

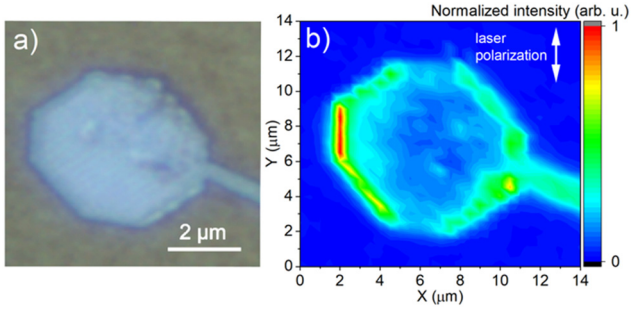

Fig. 4 (a) Optical microscope image of an octagonal-shaped structure. The trench visible on the right side was necessary to supply water beneath the h-BN surface during membrane etching. (b) False-color map of the E_{2g} Raman intensity, clearly showing that the signal enhancement occurs only on sidewalls parallel to the direction of the incoming laser polarization. The perpendicular top and bottom sidewalls do not exhibit such enhancement.

The successful fabrication of this structure allowed us to investigate whether the observed enhancement effect can be extended to other materials. To test this hypothesis, Raman spectra of the resulting structure were measured close to the edge of the membrane and on the substrate, as depicted in Fig. 3(b). Raman signals from substrate, h-BN, and graphene[43] can be observed in both spectra. The different background for the black spectrum is due to different local luminescence from point defects in h-BN. For a 532 nm laser excitation, the E_{2g} band of h-BN and the D peak from graphene overlap and are hence difficult to distinguish. To show the presence of two peaks, we conducted supplementary measurements using a 633 nm laser (see ESI†), making use of the fact that the D band energy depends on the excitation wavelength.[44] Cross sections through the membrane for polarizations parallel and perpendicular to the trench are presented in Fig. 3(c) and (d), respectively. Dashed lines were added to indicate the width of the measured membranes. The red arrow in Fig. 3(a) indicates the measurement location. Similar to the results on the pure h-BN membrane, we observed an enhancement, which shows that the effect is present also for adjacent materials. The enhancement was stronger for measurements with polarization parallel to the groove, but was also present for perpendicular polarisation.

To show that our method allows us to obtain various shapes of suspended h-BN, we fabricated octagons, as shown on the optical image in Fig. 4(a). On the corresponding Raman intensity map presented in Fig. 4(b), we again observe the characteristic h-BN peak enhancement, which is consistent with previous results. We can see that the sidewall of the octagon, which is parallel to the polarisation of the laser shows the largest enhancement. The sidewalls that are at an angle of around 45° to the laser polarization show a smaller enhancement, while the sidewalls perpendicular to the last polarization show almost no enhancement compared to the rest of the structure. An additional example of a tooth-shaped, octagonal membrane can be found in the ESI (Fig. S12†).

To correlate the spatial distribution of Raman signal from the h-BN with the electric field intensity generated in the structure, we conduct the full-wave electromagnetic simulations (implemented in Comsol). We assume a trench with infinite length in y-direction and the dimensions that correspond to the measured structure shown in Fig. 2. (810 nm depth, 700 nm-width in the germanium substrate, covered by a 30 nm-thick h-BN layer.) The structure is illuminated from the top (air region) by a normally-incident plane wave polarized either along y or in x direction (parallel and perpendicular to the trench edge, respectively). We rounded off the edges of the trench according to the measured trench profile of the germanium for the structure shown in Fig. 2. The curvature radius is 450 nm. We take the dielectric permittivity of h-BN and germanium from ref. 45 and 46, respectively. Fig. 5(a) presents a cross-section of the membrane structure. The two thin black lines on top of the trench represent the h-BN layer, while the false-colours depict the normalized absolute value of the electric field intensity ($I/I_0 = |\boldsymbol{E}|^2/|\boldsymbol{E_0}|^2$, where I_0 is the intensity on the supported h-BN) for light at the wavelength of laser excitation of 532 nm. This normalization yields a dimensionless intensity enhancement factor $F = I/I_0$ calculated with regard to the intensity on the supported h-BN layer on germanium. The plot reveals two maxima within the h-BN layer close to the rounded edges of the trench. A third maximum in the middle of the trench is situated slightly below the h-BN. The position

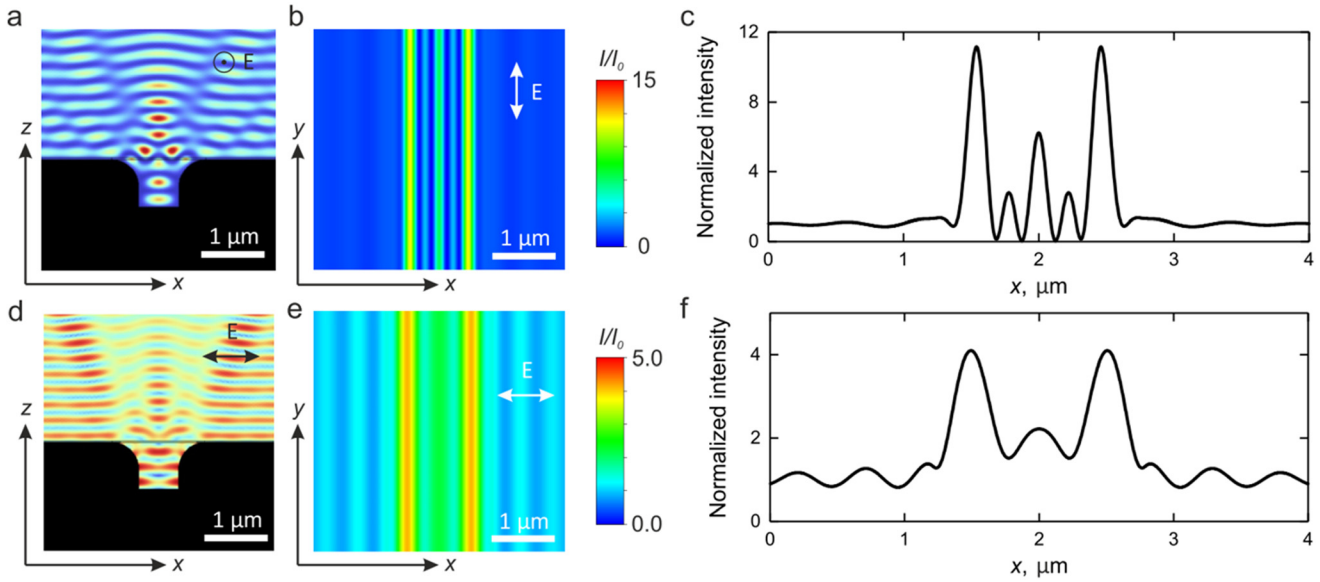

Fig. 5 Results of electromagnetic full-wave simulations. All panels represent the normalized electric field intensity, ($I/I_0 = |E|^2/|E_0|^2$, where I_0 is the intensity on the supported h-BN) for incident light at the wavelength of the laser (532 nm). (a and d) The distribution of I/I_0 as a function of *z*, *x* for the polarisation of the incident light parallel and perpendicular to the membrane edge, respectively. The black colour represents the germanium substrate; the h-BN layer on top of the trench is shown by two black horizontal lines. (b and e) The distribution of I/I_0 in the middle of the h-BN layer as a function of *x*, *y*, for parallel and perpendicular polarizations, respectively. (c and f) Display a cross-section of the distribution in b and e. Note that I/I_0 for incident light polarised perpendicular to the trench edge, is significantly weaker compared to the parallel polarisation case (compare the color scales). The simulations are in very good agreement with the experimental results presented in Fig. 2, showing that the enhancement is much larger for polarization parallel to the sidewall of the trench.

of this third maximum depends on the depth of the trench. For certain trench geometries this maximum can also be inside the h-BN layer. In this case, the enhancement factor can become even larger as for the maxima at the rounded edges. An exemplary situation in presented in the ESI.† The presence of the maxima inside the h-BN layer at the rounded edges is, however, robust also for different geometries, as demonstrated for example for the case of the octagon shaped membrane, see Fig. 4, which also shows the typical maxima at the edges parallel to the etched structure. Fig. 5(b) shows the top view (*x*–*y* plane) of the simulation of the normalized electromagnetic field intensity, which was also calculated for incident light parallel to the trench. A comparison of these simulations with the experimental Raman spectroscopy results, shown in Fig. 2(d), confirms a very good overall agreement. The additional cross section, for which the intensities were averaged over the whole h-BN thickness, presented in panel (c) illustrates the structure of enhanced lines, with a distance of around 250 nm between neighbouring peaks. Note that as mentioned earlier, the size of the laser spot in our Raman setup is about 500 nm, not allowing us to resolve these details. However, the two main maxima are in good agreement with the measurements shown in Fig. 2(b) whereas the smaller bands are washed out and contribute to the non-zero enhanced in between the peaks.

Fig. 5(d) presents a simulation for incident light polarized perpendicular to the trench edge. The normalized electric field intensity simulation presented in panel (e) clearly indicates a smaller enhancement in agreement with our Raman spectroscopy results shown in Fig. 2 and 3. Please note that in Fig. 2(c) a small Raman enhancement can also be observed for the light polarization perpendicular to the trench shape. Panel (f) suggests that the peaks are broader and slightly shifted compared to panel (c). Such subtle changes can, however, not be resolved by our setup due to laser spot limited resolution. To assess the influence of the curved edge of the trench, we additionally performed simulations of a trench with sharp edges (see Fig. S3, ESI†). In this case, the overall enhancement decreases for the parallel polarisation, and the two maxima vanish for the perpendicular case, leading to a broad maximum in the middle of the trench. Changes in the actual trench geometry hence allow to modify the spatial distribution of the field enhancement, which can be used to optimize structures, for example to selectively enhance a different spatial region of the membrane by solely changing the laser polarization. Additional simulations for the case of a single edge or a trench without an h-BN layer are presented in the ESI.† As expected, these simulations show that the presence of h-BN has a significant influence on electric field intensity. However, it is important to note that the field enhancement is not caused by h-BN itself, but rather by the response of the complex-shaped cavity covered with h-BN, which acts as a thin dielectric.

The numerical simulations clearly reproduce the overall experimental results: a strong enhancement close to the edge of the trench and a polarisation induced difference. However, to be able to set the observed Raman enhancement in relation

to the calculated electric field intensity values one has to discuss the actual mechanism of the enhancement.

To this end, we can compare our results with the case of Interference Enhanced Raman Scattering (IERS),[22–25] where the enhancement purely stems from interference effects on mirror-like substrates coated with a dielectric. In our case we do not a have a flat, translational invariant structure, but an air-filled trench with rounded edges etches covered by a continuous h-BN layer. For such a complex structure the typical transfer matrix formalism,[38] used for parallel flat layers, cannot be employed anymore and electromagnetic full-wave simulations have to be performed, as we have shown in Fig. 5. Yet, once we obtain the spatially dependent intensity enhancement factors F, the underlying Raman scattering mechanisms are the same. In agreement with the electromagnetic mechanism for SERS[47] and the formalism used for IERS,[22–25] in our case the excitation and scattering process can be treated separately. The resulting Raman enhancement factor is then calculated as the product of the intensity enhancement factor $F_{\mathrm{laser}} = I/I_0 = |\boldsymbol{E}|^2/|\boldsymbol{E_0}|^2$ of the incoming light (here 532 nm) and the intensity enhancement factor F_{Raman} at the wavelength of the scattered Raman signal (here, around 574 nm for the h-BN E_{2G} band).[23–25] To obtain an estimation for the Raman enhancement factor resulting from our numerical simulation, we performed calculations of the maximum intensity enhancement factor as a function of the wavelength (see Fig. S4 in ESI†). The product F_{laser} times F_{Raman} yields a maximum Raman enhancement factor of around 224 for the parallel polarisation and an enhancement of about 22 for the perpendicular case. This estimation should be treated as an upper limit for the observable Raman enhancement as our spatial resolution does not allow us to resolve the maximum narrow peak value, but probes a much broader area within our laser spot. We also did not take the finite numerical aperture of the objective into account, which further decreases the experimentally observable enhancement. Although the theoretical calculations overestimate the experimentally observable Raman enhancement factors, the overall agreement of the electromagnetic full-wave simulations with the Raman spectroscopy results is very good. This agreement shows that such simulations can not only can be used to explain the physical mechanisms, but also to optimize the design of h-BN/germanium microcavity structures for dedicated applications.

Conclusions

In conclusion, we demonstrated an about 10-fold Raman signal enhancement on microcavity structures consisting of a hexagonal boron nitride (h-BN) layer suspended over an air-filled trench in germanium. We successfully prepared these cavity structures by an original process of exfoliation and etching by means of photocorrosion, which allowed the fabrication of the required h-BN membranes using a standard Raman spectroscopy system. Raman mapping was performed to investigate the properties of the h-BN/germanium cavities, revealing an h-BN Raman signal enhancement close to the edge of the membrane. This effect was found to be highly dependent on the polarisation of the incident laser used for Raman measurements. Numerical simulations of the local field intensity enhancement are in very good agreement with our results reproducing both the spatial distribution of the enhancement and the polarisation dependency. The obtained electric field intensity distributions can be used to optimize the design for future applications and the structure can then be fabricated accordingly. Moreover, the electric field simulations allowed us to estimate an upper theoretical limit for Raman enhancement factors.

The h-BN membrane plays a multiple role in our approach, being part of the cavity, indicator of the Raman signal enhancement and substrate for other materials. To demonstrate the latter point, we extended our investigation to graphene bilayers deposited on the suspended h-BN. A similar Raman signal enhancement was observed for the graphene related Raman modes in the graphene/h-BN structure, which shows that the enhancement is present also for adjacent materials. By fabricating octagon-shaped membranes, we further demonstrate that different shapes of membranes can be realized by our method. For this shape, the same enhancement effect was observed, which depends on the relative orientation of the incident laser polarisation with regard to the sidewalls of the trench.

The observed effects may guide the way toward efficient Raman enhancement for materials placed on the suspended h-BN of the microcavity. Such flat, insulating, and chemically inert h-BN membrane-based cavity structures may constitute a new approach in detecting weak Raman signals, especially for 2D materials, but also for other transparent or thin biological or chemical samples.

Author contributions

Conceptualization: J. B., J. R., A. W. Investigation: J. R., K. V. V., I. N., M. T., R. B. Validation: J. B., A. W., A. Y. N., I. N., R. H., R. S., Visualization: J. R., K. L., K. V. V. Resources: A. K. D. Supervision: J. B., A. W., I. N., A. Y. N., R. H. Writing – original draft: J. R., J. B., A. W. Writing – review & editing: J. B., A. W., R. S., A. Y. N., I. N., R. H.

Data availability

Data for this article, including Raman spectroscopy data are available at Dane Badawcze UW at **https://doi.org/10.58132/QJKH8Z**.

Conflicts of interest

There are no conflicts of interest to declare.

Acknowledgements

This work was supported by the Polish National Science Centre, Poland, under decisions 2019/33/B/ST5/02766, 2020/39/D/ST7/02811, 2021/41/N/ST7/04326, 2021/41/N/ST3/03579, 2022/47/B/ST5/03314; the Spanish Ministry of Science and Innovation (grant PID2020-115221GB-C42); the Basque Department of Education (grant PIBA-2023-1-0007); "la Caixa" Foundation (ID 100010434), the fellowship code is LCF/BQ/DI21/11860026. R.H. was financially supported by the Spanish Ministry of Science and Innovation under the Maria de Maeztu Units of Excellence Program (CEX2020-001038-M/MCIN/AEI/10.13039/501100011033) and the Project PID2021-123949OB-I00/MCIN/AEI/10.13039/501100011033 by 'ERDF - A Way of Making Europe'. I.N. acknowledges financial support by the German Research Foundation (DFG) under project no. 467576442 and the Ministerium für Innovation, Wissenschaft und Forschung des Landes Nord-rhein-Westfalen.

References

1 Y. J. Lee, S. L. Vega, P. J. Patel, K. A. Aamer, P. V. Moghe and M. T. Cicerone, *issue Eng Part C Methods*, 2014, **20**(7), 562–569.
2 M. Paraskevaidi, B. J. Matthew, B. J. Holly, B. J. Hugh, C. P. V. Thulya, C. Loren, C. StJohn, G. Peter, G. Callum, K. G. Sergei, K. Kamila, K. Maria, L. M. G. Kássio, M. H. L. Pierre, P. Evangelos, P. Savithri, A. A. John, S. Alexandra, S. Marfran, S. S. Josep, T. Gunjan, W. Michael and W. Bayden, *Appl. Spectrosc. Rev.*, 2021, **56**, 804–868.
3 G. W. Auner, S. K. Koya, C. Huang, B. Broadbent, M. Trexler, Z. Auner, A. Elias, K. C. Mehne and M. A. Brusatori, *Cancer Metastasis Rev.*, 2018, **37**, 691–717.
4 L. P. Choo-Smith, H. G. M. Edwards, H. P. Endtz, J. M. Kros, F. Heule, H. Barr, J. S. Robinson, H. A. Bruining and G. J. Puppels, *Biopolymers*, 2002, **67**, 1–9.
5 E. Gerace, F. Seganti, C. Luciano, T. Lombardo, D. Di Corcia, H. Teifel, M. Vincenti and A. Salomone, *Drug Alcohol Rev.*, 2019, **38**, 50–56.
6 A. Braz, C. Santos Silva, A. C. Peixoto, M. F. Pimentel, G. Pereira, P. Caixeta Castro Souza Braga, A. L. Martini and T. Lino Fernandes Alcântara, *J. Raman Spectrosc.*, 2021, **52**, 901–913.
7 C. A. F. De Oliveira Penido, M. T. T. Pacheco, I. K. Lednev and L. Silveira, *J. Raman Spectrosc.*, 2016, **47**, 28–38.
8 A. Guirguis, S. Girotto, B. Berti and J. L. Stair, *Forensic Sci. Int.*, 2017, **273**, 113–123.
9 T. Vankeirsbilck, A. Vercauteren, W. Baeyens, G. Van der Weken, F. Verpoort, G. Vergote and J. P. Remon, *TrAC, Trends Anal. Chem.*, 2002, **21**, 869–877.
10 I. Delfino, C. Camerlingo, M. Portaccio, B. Della Ventura, L. Mita, D. G. Mita and M. Lepore, *Food Chem.*, 2011, **127**, 735–742.
11 F. Adar, R. Geiger and J. Noonan, *Appl. Spectrosc. Rev.*, 1997, **32**, 45–101.
12 Z. Xu, Z. He, Y. Song, X. Fu, M. Rommel, X. Luo, A. Hartmaier, J. Zhang and F. Fang, *Micromachines*, 2018, **9**, 361.
13 X. Xu, H. Li, D. Hasan, R. S. Ruoff, A. X. Wang and D. L. Fan, *Adv. Funct. Mater.*, 2013, **23**, 4332–4338.
14 S. Nie and S. R. Emory, *Science*, 1997, **275**, 1102–1106.
15 E. J. Blackie, E. C. Le Ru and P. G. Etchegoin, *J. Am. Chem. Soc.*, 2009, **131**, 14466–14472.
16 T. Deckert-Gaudig, A. Taguchi, S. Kawata and V. Deckert, *Chem. Soc. Rev.*, 2017, **46**, 4077–4110.
17 N. Kumar, B. M. Weckhuysen, A. J. Wain and A. J. Pollard, *Nat. Protoc.*, 2019, **14**, 1169–1193.
18 E. A. Pozzi, M. D. Sonntag, N. Jiang, J. M. Klingsporn, M. C. Hersam and R. P. Van Duyne, *ACS Nano*, 2013, **7**, 885–888.
19 T. M. Willey, A. L. Vance, T. Van Buuren, C. Bostedt, L. J. Terminello and C. S. Fadley, *Surf. Sci.*, 2005, **576**, 188–196.
20 J. F. Li, Y. F. Huang, Y. Ding, Z. L. Yang, S. B. Li, X. S. Zhou, F. R. Fan, W. Zhang, Z. Y. Zhou, D. Y. Wu, B. Ren, Z. L. Wang and Z. Q. Tian, *Nature*, 2010, **464**, 392–395.
21 Y. J. Zhang, H. Ze, P. P. Fang, Y. F. Huang, A. Kudelski, J. Fernández-Vidal, L. J. Hardwick, J. Lipkowski, Z. Q. Tian and J. F. Li, *Nat. Rev. Methods Primers*, 2023, **3**, 1–18.
22 R. J. Nemanich, C. C. Tsai and G. A. N. Connell, *Phys. Rev. Lett.*, 1980, **44**, 273.
23 D. Solonenko, O. D. Gordan, A. Milekhin, M. Panholzer, K. Hingerl and D. R. T. Zahn, *J. Phys. D: Appl. Phys.*, 2016, **49**, 115502.
24 K. Liu, K. Liu, K. Liu, T. Gong, T. Gong, Y. Luo, Y. Luo, W. Kong, W. Kong, W. Yue, W. Yue, C. Wang, C. Wang, X. Luo and X. Luo, *Opt. Express*, 2023, **31**, 15848–15863.
25 D. Yoon, H. Moon, Y. W. Son, J. S. Choi, B. H. Park, Y. H. Cha, Y. D. Kim and H. Cheong, *Phys. Rev. B:Condens. Matter Mater. Phys.*, 2009, **80**, 125422.
26 A. Laturia, M. L. Van de Put and W. G. Vandenberghe, *npj 2D Mater. Appl.*, 2018, **2**, 1–7.
27 F. Hui, C. Pan, Y. Shi, Y. Ji, E. Grustan-Gutierrez and M. Lanza, *Microelectron. Eng.*, 2016, **163**, 119–133.
28 A. Azizi, M. R. Gadinski, Q. Li, M. Abu AlSaud, J. Wang, Y. Wang, B. Wang, F. Liu, L.-Q. Chen, N. Alem, Q. Wang, A. Azizi, M. R. Gadinski, Q. Li, M. A. AlSaud, J. Wang, Y. Wang, B. Wang, F. Liu, L. Chen, N. Alem and Q. Wang, *Adv. Mater.*, 2017, **29**, 1701864.
29 D. Chu, S. W. Pak and E. K. Kim, *Sci. Rep.*, 2018, **8**, 1–8.
30 N. Kostoglou, K. Polychronopoulou and C. Rebholz, *Vacuum*, 2015, **112**, 42–45.
31 C. R. Dean, A. F. Young, I. Meric, C. Lee, L. Wang, S. Sorgenfrei, K. Watanabe, T. Taniguchi, P. Kim, K. L. Shepard and J. Hone, *Nat. Nanotechnol.*, 2010, **5**, 722–726.
32 F. Cadiz, E. Courtade, C. Robert, G. Wang, Y. Shen, H. Cai, T. Taniguchi, K. Watanabe, H. Carrere, D. Lagarde, M. Manca, T. Amand, P. Renucci, S. Tongay, X. Marie and B. Urbaszek, *Phys. Rev. X*, 2017, **7**, 021026.

33 K. Ludwiczak, A. K. Dąbrowska, J. Kucharek, J. Rogoza, M. Tokarczyk, R. Bozek, M. Gryglas-Borysiewicz, T. Taniguchi, K. Watanabe, J. Binder, W. Pacuski and A. Wysmolek, *ACS Appl. Mater. Interfaces*, 2024, **16**, 49710.
34 A. Dabrowska, M. Tokarczyk, G. Kowalski, J. Binder, R. Bo, J. Borysiuk, R. Ste and A. Wysmolek, *2D Mater.*, 2020, **8**, 015017.
35 M. Tokarczyk, A. K. Dabrowska, G. Kowalski, R. Bozek, J. Iwanski, J. Binder, R. Stepniewski and A. Wysmolek, *2D Mater.*, 2023, **10**, 025010.
36 J. Binder, J. Rogoza, L. Tkachenko, I. Pasternak, J. Sitek, W. Strupinski, M. Zdrojek, J. M. Baranowski, R. Stepniewski and A. Wysmolek, *2D Mater.*, 2021, **8**, 35043.
37 J. Iwanski, A. K. Dabrowska, M. Tokarczyk, J. Binder, R. Stepniewski and A. Wysmolek, *Acta Phys. Pol., A*, 2021, **139**, 457–461.
38 B. A. Weinstein and M. Cardona, *Phys. Rev. B*, 1973, **7**, 2545.
39 R. Geick, C. H. Perry and G. Rupprecht, *Phys. Rev.*, 1966, **146**, 543.
40 A. K. Dabrowska, J. Binder, I. Prozheev, F. Tuomisto, J. Iwanski, M. Tokarczyk, K. P. Korona, G. Kowalski, R. Stepniewski and A. Wysmolek, *J. Lumin.*, 2024, **269**, 120486.
41 I. Pasternak, A. Krajewska, K. Grodecki, I. Jozwik-Biala, K. Sobczak and W. Strupinski, *AIP Adv.*, 2014, **4**, 097133.
42 J. Kierdaszuk, P. Dabrowski, M. Rogala, P. Krukowski, A. Przewloka, A. Krajewska, W. Kaszub, M. Sobanska, Z. R. Zytkiewicz, V. Z. Zubialevich, P. J. Kowalczyk, A. Wysmolek, J. Binder and A. Drabinska, *Carbon*, 2022, **186**, 128–140.
43 A. C. Ferrari, J. C. Meyer, V. Scardaci, C. Casiraghi, M. Lazzeri, F. Mauri, S. Piscanec, D. Jiang, K. S. Novoselov, S. Roth and A. K. Geim, *Phys. Rev. Lett.*, 2006, **97**, 187401.
44 L. M. Malard, M. A. Pimenta, G. Dresselhaus and M. S. Dresselhaus, *Phys. Rep.*, 2009, **473**, 51–87.
45 D. V. Grudinin, G. A. Ermolaev, D. G. Baranov, A. N. Toksumakov, K. V. Voronin, A. S. Slavich, A. A. Vyshnevyy, A. B. Mazitov, I. A. Kruglov, D. A. Ghazaryan, A. V. Arsenin, K. S. Novoselov and V. S. Volkov, *Mater. Horiz.*, 2023, **10**, 2427–2435.
46 T. N. Nunley, N. S. Fernando, N. Samarasingha, J. M. Moya, C. M. Nelson, A. A. Medina and S. Zollner, *J. Vac. Sci. Technol., B:Nanotechnol. Microelectron.:Mater., Process., Meas., Phenom.*, 2016, **34**, 61205.
47 *Surface-Enhanced Raman Scattering*, ed. K. Kneipp, M. Moskovits and H. Kneipp, Springer, Berlin Heidelberg, 2006, vol. 103.

